Elastic models: a comparative study applied to retinal images

E.Karali[1], S. Lambropoulou[2], and D. Koutsouris[1]

1. National Technical University of Athens, Department of Electrical and Computer Engineering, Biomedical Engineering Laboratory, Zografou Campus, Athens, Greece

2. National Technical University of Athens, School of Applied Mathematical and Physical Sciences, Department of Mathematics, Zografou Campus, Athens, Greece

Corresponding author: Dr. E. Karali

email: ekarali@biosim.ntua.gr

Elastic models: a comparative study applied to retinal images

Abstract

In this work various methods of parametric elastic models are compared, namely the classical snake, the gradient vector field snake (GVF snake) and the topology-adaptive snake (t-snake), as well as the method of self-affine mapping system as an alternative to elastic models. We also give a brief overview of the methods used. The self-affine mapping system is implemented using an adapting scheme and minimum distance as optimization criterion, which is more suitable for weak edges detection. All methods are applied to glaucomatic retinal images with the purpose of segmenting the optical disk. The methods are compared in terms of segmentation accuracy and speed, as these are derived from cross-correlation coefficients between real and algorithm extracted contours and segmentation time, respectively. As a result, the method of self-affine mapping system presents adequate segmentation time and segmentation accuracy, and significant independence from initialization.

Keywords: image segmentation, snakes, GVF snakes, T-snakes, self affine mapping system

I. Introduction

Image segmentation is an important preprocessing step in the field of medical imaging. It is used especially in automatic anatomical structure and pathological areas detection. Image segmentation has been used in diagnoses and detection of pathologies, in quantization of tissue volume, in planning therapy, in computer-integrated surgery, in the correction of partial volume in PET, in the detection of coronary arteries in angiographies, in automatic classification of blood cells, in mapping brain functions, etc [1].

Because of the variety of object shapes and the variance in image quality, image segmentation remains a difficult task. There does not exist a catholic image segmentation method that can be applied with success in any imaging study. Every segmentation algorithm aims at the detection of the image pixels that belong to the object of interest. The methods that try to detect the area of an object rely on the intensity or texture values of image pixels, while the segmentation techniques that search for object boundaries use the image derivatives that present high values near the object boundaries.

Elastic models are the most popular image segmentation techniques. They are designed to approximate the significant variance of biological structures with time and from person to person. Elastic models are curves or surfaces defined on image domain that deform under the influence of internal and external forces. Internal forces are related to the curve or the surface itself and are designed to keep the model smooth during the deformation process. External forces adjust the model to the real object boundary and their computation is based on image information and. In theory, because of the constrain for smooth contours and their ability to incorporate a priori information for object shape, elastic models can handle noise problems in images and contour discontinuities. So, they permit the

description of the contour as a continuous mathematical model and they are able to achieve inter-pixel segmentation accuracy.

In the bibliography elastic models can be found as deformable models, active contours or surfaces and snakes. The mathematical foundation of elastic models is based on a contribution of geometry, physics and approximation theory. Object shape is represented by geometric lows. Physics apply constrains in the deformation process through space and time. Approximation theory offers the fitting mechanisms of the model to the real object boundary. Most elastic models are connected to an energy function that is determined according to the geometrical degree of freedom. The energy function increases as the model draws away from the real boundary. Usually the energy function contains terms related to the elastic forces internal to the model. Approximation theory imposes another energy term, the function of external forces that create an external energy field.

Elastic models are divided into parametric elastic models and geometric elastic models. Parametric models are parametric curves or surfaces that evolve according to the Lagrange equation. Geometric models present curves or surfaces as the level sets of higher-dimensional scalar functions. Geometric models evolve according to the curve evolution theory [2].

In this work various methods of parametric elastic models are presented, namely, the classical snake [3][4][5][6], the gradient vector field snake (GVF snake)[7][8][9][10] and the topology-adaptive snake (t-snake)[11][12][13][14]. Also, the method of self-affine mapping system[15][16] is presented as an alternative of the elastic models. The self-affine mapping system is implemented using an adapting scheme for determining the size of areas with similarity, and minimum distance as optimization criterion which, according to Section III.a (Results), is more suitable for weak edges detection. All methods are applied

to glaucomatic retinal images with the purpose of segmenting the optical disk. Moreover, the aforementioned methods are compared in terms of segmentation accuracy.

The optical disk is the optical nerve and the vessels' entrance point in the retina. In fundus gray images it appears as a luminous white area. It has an almost round shape that is interrupted by the outgoing vessels. Some times the optical disk has an elliptical shape because of the small but not negligible angle between the planes of the image and the object. Optical disk size varies from patient to patient.

Optical disk segmentation consists in a very important preprocessing stage of many algorithms, which have been designed for automatic detection of retinal anatomical structures and pathological conditions. For example the detection methods of some vessels and their junctions start from the optical disk area, where the big vessels lie. These can serve as starting points for the detection of the other vessels[17]. Also, macula's position usually is estimated according to the optical disk's position under the condition that the distance between the macula and the optical disk is constant [18][19]. Moreover, optical disk camouflage contributes to better and easier lesions detection related to different retinopathies [20]. Furthermore, the optical disk center can be used as a reference point for distance measurements in retinal images. In addition, the optical disk can be a reference area for the registration of retinal images acquired in different time or with a different method. Retinal images registration can reveal changes in vessels' size and disposition inside the optical disk, as well as changes in optical disk size related to serious eye diseases, such as glaucoma and vessels neoplasia[21].

In Section II some theoretical aspects of the methods under comparison are presented. The results of the comparison are presented in Section III and are analyzed in Section IV. Section V contains the conclusions.

II Elastic Models Segmentation Methods

In this part we give an overview of four methods for image segmentation: the classical snake, the gvf snake, the t-snake and the self-affine mapping system. In sections B and C we will be using the notation introduced in section A.

A. Classical Snake

The classical snakes are used widely in image processing, in computer vision and in medical imaging applications for allocating object boundaries. The classical parametric elastic models (classical snakes), due to Kass, Witkin and Terzopoulos[3] change shape and finally are adapted to the real object boundary according to the minimization process of an energy function. The energy function reaches its global minimum when the active contour is smooth and coincides with the real object boundary [3][4][5][6]. An active contour is represented by a curve $\vec{X}(s) = (x(s), y(s))$ in 2D or a surface $\vec{X}(s) = (x(s), y(s), z(s))$ in 3D, $s \in [0,1]$. Active contours crawl like snakes on the image plane or space with the purpose of energy minimization. The energy function is defined as:

$$E(\vec{X}) = S(\vec{X}) + P(\vec{X}) \quad (1)$$

The term $S(\vec{X})$ is the function of internal energy, defined as:

$$S(\vec{X}) = \frac{1}{2}\int_0^1 \left(a(s)\left|\frac{\partial \vec{X}}{\partial s}\right|^2 + \beta(s)\left|\frac{\partial^2 \vec{X}}{\partial s^2}\right|^2 \right) ds \quad (2).$$

The factor $a(s)\left|\frac{\partial \vec{X}}{\partial s}\right|^2$ constrains the model to act as an elastic membrane, so it determines contour elasticity. The factor $\beta(s)\left|\frac{\partial^2 \vec{X}}{\partial s^2}\right|^2$ enforces the model to act like a rigid body, so it

determines the rigidity of the model. Parameters $a(s)$ and $\beta(s)$ specify elasticity and rigidity levels of the model respectively. In general, coefficients a and β are able to change with time and along the active contour. In most applications they are positive constants. The term $P(\vec{X})$ in Eq. 1 is the function of the dynamic energy defined as:

$$P(\vec{X}) = \int_0^1 P(\vec{X}(s))ds \quad (3)$$

The function $P(\vec{X})$ is determined according to image data I. In the case of a 2D image its typical form is:

$$P(x,y) = -w\left|\nabla\left(G_\sigma(x,y) * I(x,y)\right)\right|^2 \quad (4)$$

where w a positive constant and $G_\sigma(x,y)$ a 2D Gaussian with standard deviation σ. Actually, $\nabla P(\vec{X})$ represents the external Gaussian potential force F_G, which pushes the snake to the true object boundary when the initial snake model is placed near the real object contour. Its range depends on the value of σ. Big values of σ increase the force's range but blur and adulterate the final contour.

Another external force that is widely used in snake applications is pressure force F_p determined as: $F_p = w_p \vec{N}(\vec{X})$ (5)

where $\vec{N}(\vec{X})$ the unit vector perpendicular to the snake in position $\vec{X}$ with direction inwards the snake curve, and w_p a constant that determines whether the pressure force will contract or dilate the snake. The value of w_p must be such that the pressure force is slightly smaller than the Gaussian potential force. Also, the value of w_p ought to be large enough, so as the snake model to avoid weak or false edges.

The curve that minimizes the energy $E(\vec{X})$ satisfies the Lagrange equation:

$$\frac{\partial}{\partial s}\left(a\frac{\partial \vec{X}}{\partial s}\right)-\frac{\partial^2}{\partial s^2}\left(\beta\frac{\partial^2 \vec{X}}{\partial s^2}\right)-F_G-F_p=0 \quad (6)$$

Other external forces are distance potential force and interactive forces.

B. Gradient Vector Flow Snake (GVF snake)

The use of classical snake is unfortunately limited because they must be initialized close to the true contour and because of their inefficient convergence in boundary concavities. Xu and Prince proposed an improved snake model in order to overcome classical snakes' limitations[7]. In particular, they introduced a new external force, the gradient vector flow (GVF), that is computed as the diffusion of gradient vectors of a gray or binary edge map of the image. According to Xu and Prince, the usual external forces are conservative forces that make the active contour unable to successfully approximate boundary concavities. GVF is a non-conservative force. Mathematically, it is based on the Helmholtz theorem, according to which a general static vector field can be separated in a conservative and tubular field. GVF snakes were designed to have conservative and tubular characteristics in order to present the desirable properties of adequate initialization range and convergence in boundary concavities [7][8][9]. Suppose that $F_{ext}=v(x,y)$ is the new GVF external force. Then, according to the force equilibrium:

$$a\frac{\partial^2 \vec{X}(s,t)}{\partial s^2}-\beta\frac{\partial^4 \vec{X}(s,t)}{\partial s^4}+\vec{v}(\vec{X}(s,t))=0 \quad (7)$$

In GVF snakes also defined an edge map $f(x,y)$ computed by image data. The edge map presents high values near image edges. For gray images the edge map is defined as

$f(x,y) = |\nabla I(x,y)|$ or $f(x,y) = |\nabla[G_\sigma(x,y) * I(x,y)]|$, the latter in case of gray images with high noise levels. The GVF field determined as $\vec{v}(x,y) = [u(x,y), \upsilon(x,y)]$ minimizes the energy function:

$$\mathrm{E} = \iint \mu\left(u_x^2 + u_y^2 + \upsilon_x^2 + \upsilon_y^2\right) + |\nabla f|^2 |\vec{v} - \nabla f|^2 \, dxdy \quad (8)$$

where μ is the linear or surface mass density. With the help of calculus variations analysis the GVF field is computed by solving the following Euler equations:

$$\left.\begin{aligned} \mu\nabla^2 u - (u - f_x)\left(f_x^2 + f_y^2\right) = 0 \\ \mu\nabla^2 \upsilon - (\upsilon - f_y)\left(f_x^2 + f_y^2\right) = 0 \end{aligned}\right\} \quad (9)$$

If u and υ are functions of time, the solution of Eq. 8 is:

$$\left.\begin{aligned} u_t(x,y,t) = \mu\nabla^2 u(x,y,t) - (u(x,y,t) - f_x(x,y))\left(f_x(x,y)^2 + f_y(x,y)^2\right) \\ \upsilon_t(x,y,t) = \mu\nabla^2 \upsilon(x,y,t) - (\upsilon(x,y,t) - f_y(x,y))\left(f_x(x,y)^2 + f_y(x,y)^2\right) \end{aligned}\right\} \quad (10)$$

C. Topologically Adaptable Snake (T-snake)

T-snakes comprise another variant of classical snakes. They are based on a space partitioning technique to create topologically adaptable snakes. The difference between the classical snake and T-snake is the use of an affine cell image decomposition, so as to iteratively reparametrize the snake and to make topological transformations. Image is partitioned into a net of discrete triangular cells. As the snake evolves under the influence of internal and external forces, it is reparametrized with a new set of nodes and elements. The reparametrization process consists of an efficient calculation of the intersections of the snake with the image net. These intersection points might be nodes of the updated T-snake. In 2D the T-snake is a 2D curve consisting of N nodes connected in series. The T-snake is

a discrete version of the classical snake and retains many of its properties [11][12][13][14]. The nodes have time varying positions $\vec{X}_i = [x_i(t), y_i(t)]$, $i = 1,2,...,N$. The snake is deformed according to elastic forces $a_i(t)$, rigidity forces $\beta_i(t)$, pressure forces $\rho_i(t)$ and external forces $f_i(t)$ that act on the image field. In order to generate a closed curve a periodic constrain is applied, namely $\vec{X}_1 = \vec{X}_N$. The overall performance of the snake is based on a discrete and simplified equation of equilibrium:

$$\vec{a}_i + \vec{\beta}_i = \vec{\rho}_i + \vec{f}_i \quad (11)$$

The pressure force $\rho_i(t)$ is used as an external force to push the snake towards image edges until it is compensated by the external force $f_i(t)$. Pressure force is defined as:

$$\vec{\rho}_i = qF(I(x,y))\vec{n}_i \quad (12)$$

where $\vec{n}_i$ is the unit normal vector to the snake at node i, and q the amplitude of the force. F is a binary function that connects the pressure force with image data:

$$\left.\begin{array}{l} F(I(x,y)) = +1, \quad if \quad I(x,y) \geq T \\ F(I(x,y)) = -1, \quad if \quad I(x,y) < T \end{array}\right\} \quad (13)$$

where T is an image intensity threshold. The function F makes the T-snake contract when $I(x,y) < T$ and is used to prevent the snake from leaking into the background. To stop the snake at significant edges there is another external force included, $f_i(t)$, which is a force based on a Gaussian potential field:

$$\vec{f}_i = -p\left|\nabla\left(G_\sigma(x,y) * I(x,y)\right)\right|^2 \quad (14)$$

The weights p and q are usually chosen to be of the same order, with p slightly larger than q, so a significant edge will stop inflation, but q is large enough, so that the snake

will pass from spurious edges without stopping at them. The update step of node position between time t and $t + \Delta t$ is:

$$\vec{X}_i^{t+\Delta t} = \vec{X}_i^t - \frac{\Delta t}{\gamma}\left(a\vec{a}_i^t - b\vec{\beta}_i^t - \vec{\rho}_i^t - \vec{f}_i^t\right) \quad (15)$$

with a and b being constants. Eq. 15 is unstable, unless small time steps are used. However, it is efficient, simple and can handle a variety of time steps that can create a stable T-snake behavior, and so an accurate segmentation result.

During the reparametrization step the interior of the snake is monitored by turning on any vertex of the image net cells from which the snake passes. Because of the net, the snake model is capable of topological transformations. This allows the snake to be independent of initial positioning, to crawl, and to efficiently attach to complicated object shapes with complicated topology in a stable manner. T-snakes combine space partitioning, internal reparametrization and topological flexibility of a geometric model with the properties of a parametric model.

D. Self-Affine Mapping System

The self-affine mapping system is a technique similar to the snake model that adjusts an initial curve to the real object contour, using a self-affine mapping system which is used widely in fractal encoding. This particular method has an advantage over conventional snakes, mostly because of its ability to detect distinct and blurred edges with significant accuracy. It has replaced the process of energy minimization of the classical snake with a contractive self-affine mapping system that is used in the creation of fractal shapes. The parameters of the system are determined after a blockwise self-similarity analysis of the

gray image through a simplified algorithm of fractal coding. The use of the self-affine mapping system is due to the fact that the points of the initial map, when they are positioned near image edges after iterative contractions of the map, they are finally attached to the edges. This attraction can be exploited for contour extraction that has the shape of a curve of similar points rather than a curve of smooth points which are detected by the snake model [15][16].

Suppose an image $g(\mathbf{x})$ is defined in $G \subset R^n$. If there exist affine transformations $a_i : A_i \to R^n$ and $\beta_i : R^1 \to R^1$ so that

$$\forall\ x \in A_i,\ g(\mathbf{x}) = \beta_i(g(a_i(\mathbf{x}))), i = 1,2,...,I \quad (16)$$

for some image regions $A_i \subset G$, then the texture in A_i is similar to the texture in $a_i(A_i)$ and the image presents self-similarity in these two regions. The set $\{A_i, a_i, \beta_i \mid i = 1,2,..,I\}$, where I is the total number of regions A_i, is called self-affine model of the image. If Eq. 16 holds then the following is also true:

$$\forall\ \mathbf{x} \in a_i(A_i),\ g(\mathbf{x}) = \beta_i^{-1}(g(a_i^{-1}(\mathbf{x}))), i = 1,2,...,I \quad (17)$$

giving rise to another self-affine model, $\left\{a_i(A_i), a_i^{-1}, \beta_i^{-1} \mid i = 1,2,..,I\right\}$ of the image the set. The transformations a_i dilate maps and β_i contract maps.

If Ω is the set of subsets of G then the self-affine map $S : \Omega \to \Omega$ is defined as:

$$S(X) = \left\{ \bigcup_{i=1}^{I} a_i(A_i \cap X) \right\} \cup C \quad (18)$$

where X is a subset of G and C a fixed set. When X is known its intersection with A_i is mapped through the affine transformation a_i and the union of all these mapped regions with C results in the final map $S(X)$.

For a 2D image $n = 2$, A_i are squared image regions, subsets of G, and transformations a_i are defined as:

$$\forall x \in A_i, a_i(\mathbf{x}) = r_i(\mathbf{x} - \bar{x}_i) + (\tau_i + \bar{x}_i) \quad (19)$$

and

$$r_i > 1 \quad (20)$$

where $\bar{x}_i$ the central point of A_i. Moreover, the self-affine model assumes that:

$$\beta_i(g(a_i(\mathbf{x}))) = p_i g(a_i(\mathbf{x})) + q_i, p_i \in [0,1] \quad (21)$$

In order for map S to be determined, the regions A_i are first defined. Then an adequate algorithm searches for the best values of the parameters r_i, p_i, q_i and $\tau_i = (s_i, t_i)$ of the map, so that Eq. 20 is satisfied for every A_i and, consequently, the self-affine models $\{A_i, a_i, \beta_i\}$ and $\left\{a_i(A_i), a_i^{-1}, \beta_i^{-1}\right\}$ are determined. The searching is performed through a block-matching algorithm. The block-matching algorithm consists of the following steps:

STEP 1: Initialization of r, s and t. Moreover, the difference $E = g(\mathbf{x}) - \beta_i(g(a_i(\mathbf{x})))$ is assigned a very large value.

STEP 2: For every $\mathbf{x} \in A_i$ the value of $g(a_i(\mathbf{x}))$ is computed. Because the sampling points $\mathbf{x}$ may be between image pixels, the values $g(a_i(\mathbf{x}))$ are computed using bilinear interpolation.

STEP 3: Initialization of p and q.

STEP 4: Computation of $\beta_i(g(a_i(\mathbf{x})))$ for every $\mathbf{x} \in A_i$.

STEP 5: Computation of the difference E. For this computation the Mean Square Error (MSN) or the Absolute Mean Distance (AMD) are usually used. If the new E is smaller than the initial value, then the initial value is replaced by the new E, and the values of r, s, t, p and q are registered as r_i, s_i, t_i, p_i and q_i respectively.

STEP 6: If all p and q are checked then the algorithm moves to STEP 7, otherwise it goes back to STEP 4.

STEP 7: If all r, s, and t are checked the algorithm is terminated, otherwise it goes back to STEP 2.

As in the conventional snake model, this method must be initialized by a rough contour. The pixels inside the initial curve take value 1 and the rest belong to the background having value 0. This way a binary image is created, called alpha mask. The purpose of the self-affine mapping system is the fitting of the alpha mask contour to the real object boundary. In order for the initial curve b to be attached to the real contour c three conditions must be satisfied:

1. the set c must equal the invariable set S,
2. the transformations a_i^{-1} must be systolic,
3. the set b should be adequately close to c.

Moreover, parameters s,t which are defined during the block-matching process should be determined, so that every set $a_i(A_i)$ contains the corresponding A_i, namely: $-\frac{r-1}{2}e \le s,t \le \frac{r-1}{2}e$, where e is the size of regions A_i. Finally, the total number of iterations ν should be: $\nu > \frac{\log\frac{e}{2}}{\log r}$.

III. Results

a. A New Self-Affine Mapping System optimization criterion.

In the self-affine mapping system the size of the areas $a_i(A_i)$ was chosen to be twice the size of the areas A_i, namely $r = 2$ so as condition 2 to holds. The searching area for the block-matching process was $[-\frac{n}{4}, \frac{n}{4}]$, where n the size of the area A. When the value of n is small (e.g. $n = 8$) condition 3 is not satisfied, while when it is large (e.g. $n = 32$) condition 3 is satisfied, but the final contour is a rough approximation of the optic disk true boundary and condition 1 is now not satisfied and fine details of the object's boundary are not detected. So, we chose an adapting scheme where n is assigned an initial big value ($n = 32$), which is gradually decreased to $n = 4$, namely $e_{\max} = 32$ and $e_{\min} = 4$. The number of iterations was set to $\nu = \frac{\log \frac{e}{2}}{\log r} + 1$. In Eq. 21 p was set to 1 and q to 0. As optimization criteria of measuring the difference between $g(x)$ and $\beta_i(g(a_i(x)))$, two criteria were tested and optically evaluated. The first was the classical AMD and the second was the Minimum Distance (MD).

Fig. 1 presents the final contours using $n = 8$ και $n = 32$ fused in the same optical image (Fig. 1a), and the final contour using the adapting scheme (Fig.1b).

From Fig.1b one can observe the strong attraction of mask boundary points from the vessels in the area of the optic disk. Vessels are strong edges. The AMD function is minimized towards these strong edges and the mask boundary points are caged from the edges of the vessels. Fig.2 shows a self-affine mapping system application, where MD was used instead of AMD. The application of MD results in the detection of optic disk boundary and not the detection of points that belong to strong edges, like the vessels.

However, the detection of weak edges reduces the degrees of freedom in mapping out the initial contour. Thus, MD is preferable for weak edges detection.

b. Comparison of elastic models

The different segmentation methods were applied to 26 glaucomatic retinal images 512x512 pixels in size, in order for the optic disk boundary to be extracted. The aforementioned optical disk segmentation techniques were applied to glaucomatic retinal images. Glaucoma results in local vessel deformations inside the optical disk. To detect such deformations with time image registration must be performed. Such a registration process consists of two steps. The first step uses global transformation for the area outside the optical disk, while the second applies local transformations for the area inside the optical disk. Hence, optical disk segmentation is a necessary preprocessing step.

For the implementation of the classical snake the external force derived from a Gaussian potential field with $\sigma = 3$ was used, accompanied with a pressure force with constant weights. In every position of the snake nodes, external force values were calculated using the bilinear interpolation method. Constant weights were also used for the internal forces. Initial contours were placed close to the real object boundary.

The GVF field was calculated according to the equations:

$$u_{i+1} = u_i + \mu 4\nabla^2 u_i - |\nabla f|(u_i - f_x) \quad (22)$$

$$\upsilon_{i+1} = \upsilon_i + \mu 4\nabla^2 \upsilon_i - |\nabla f|(\upsilon_i - f_y) \quad (23)$$

were f_x and f_y are the first derivatives of the edge map f of the image I. The edge map was derived as $f(x,y) = |\nabla[G_\sigma(x,y) * I(x,y)]|$, with $\sigma = 3$. Initial values for u and

υ were $u_{init} = f_x$ and $\upsilon_{init} = f_y$. Moreover, μ was set to 0.29 and 80 total iterations were used for the calculation of the GVF field for all the 26 applications. Initial contours were placed close to the real ones. The GVF field was accompanied by a Gaussian potential and a pressure force and all together constituted the general external energy field.

T-snakes were implemented according to Eq. 11. For the implementation of the T-snake the external force derived from a Gaussian potential field with $\sigma = 3$ was used, accompanied with a pressure force with constant weights. The initial seed point was chosen to be inside the object of interest. According to this seed point the algorithm initializes a square snake.

In the self-affine mapping system the size of the areas $a_i(A_i)$ was chosen to be twice the size of the areas A_i, namely $r = 2$, so as condition 2 to hold. The searching area for the block-matching process was $[-\frac{n}{4}, \frac{n}{4}]$, where n the size of the area A. As a criterion of measurement, minimum distance was used to calculate the difference between $g(x)$ and $\beta_i(g(a_i(x)))$. The number of iterations was set to $\nu = \frac{\log \frac{e}{2}}{\log r} + 1$. In Eq. 21 p was set to 1 and q to 0.

Fig.3 presents comparatively optic disk extraction using the classical snake model, the GVF model, the T-snake and the self- affine mapping system. Manual segmentation of the optical disk is also presented in Fig.3 for visual comparison with the aforementioned automated methods.

For the comparative evaluation of the different deformable models cross-correlation coefficient between the real optic disk contour and the final contour extracted by every deformable model method was applied to the 26 retinal images. The real contours were

drawn by an expert. The cross-correlation coefficient was calculated according to the equation:

$$c = \frac{\sum_{i=1}^{N}\sum_{j=1}^{N}(I_{deformable_{ij}} - \bar{I}_{deformable})(I_{real_{ij}} - \bar{I}_{real})}{\sqrt{\sum_{i=1}^{N}\sum_{j=1}^{N}(I_{deformable_{ij}} - \bar{I}_{deformable})^2 \sum_{i=1}^{N}\sum_{j=1}^{N}(I_{real_{ij}} - \bar{I}_{real})^2}} \quad (24)$$

Fig.4 presents cross-correlation coefficients for the four deformable model techniques and for the 26 retinal images.

Finally, Fig.5 shows the total segmentation time for the four deformable models for the 26 retinal images.

IV. Discussion

From Fig.3 it can be seen that the classical snake presents slightly superior behavior in comparison to GVF snake. The final contour of the classical model is smooth and approximates better the real one. GVF snakes is an alternative of the classical snake designed to detect complicated boundaries with high curvature and sharp edges. But the optic disk boundary does not have such characteristics, it is almost round. The range of the two methods is almost the same. The classical snake and the GVF snake must be initialized close to the real contour. According to Fig.4 the GVF snake algorithm is also slower than the classical snake method, mostly because of the extra time it needs to calculate the external GVF force.

T-snakes result in a satisfying optic disk contour, although the classical snake seems to be slightly better (Fig. 3b and e). The biggest advantage of the T-snake algorithm is its range. It is initialized in a point inside the optic disk. Moreover, the total segmentation

time of T-snake is small, smaller than any other deformable method. So, T-snake presents a robust and efficient segmentation technique.

Finally, the self-affine mapping system is superior in optic disk boundary extraction than the other techniques, according to Fig. 3. Furthermore, the algorithm is independent from optic disk size and image intensity. Also, with the choice of minimum distance as a matching criterion, the caging of the model from the vessels is avoided. The self-affine mapping system seems to present lower independence from initialization than the classical snake and the GVF snake. The initial contour is placed slightly away from the real one (Fig.6b). The total segmentation time of the algorithm is also adequate according to Fig. 5, since it is faster than the classical snake and the GVF snake. The self-affine mapping system succeeds also in high cross-correlation values (Fig. 4) similarly to the classical snake and the GVF snake, which, though, have been initialized close to the real boundary in order to achieve such cross-correlation values. T-snakes present smaller cross-correlation values because they are not initialized close to the real optic disk contour. Another advantage of the self-affine mapping system is that this method is self-terminated, a characteristic that the other deformable methods do not present.

In general the self-affine mapping system succeeds in approximating very well the true optic disk boundary. However, the initial contour must be close to the true. The distance between the real and the initial contour depends on the value of $e_{\max}$. If $e_{\max}$ is increased the degrees of freedom in lining the initial contour are increased but the algorithm's computation cost is augmented.

V. Conclusions

In this work various methods of parametric elastic models were compared, namely the classical snake, the gradient vector field snake (GVF snake) and the topology-adaptive snake (t-snake). Also, the method of self-affine mapping is presented as an alternative of the elastic models. The self-affine mapping system was implemented using an adapting scheme. Moreover, Minimum Distance was introduced as an optimization criterion more suitable for optic disk boundary detection. All methods were applied to glaucomatic retinal images with the purpose of segmenting the optical disk. The methods are compared in terms of segmentation accuracy. The self-affine mapping system presents efficient segmentation time, segmentation accuracy and significant independence from initialization.

VI References

[1]. C. Xu, D.Pham and J. Prince, Image Segmentation Using Deformable Models, ch.3, in: *SPIE Handbook on Medical Imaging*, *Vol III: Medical Image Analysis*, J.M. Fitzpatrick and M. Sonka, May 2000.

[2]. C. Xu, A.Yezzi and J. Prince, On the Relationship between Parametric and geometric Active Contours, *Proc. Of the 34th Asilomar Conference on Signals, Systems and Computers*, 2000, 483-489.

[3]. M. Kass, A. Witkin and D. Terzopoulos, Snakes: Active Contour Models, *International Journal of Computer Vision*, 1988, 321-331.

[4]. T. McInerney and D. Terzopoulos, Deformable models in medical image analysis: a survey, *Medical Image Analysis*, Vol 1, No 2, 1996, 91-108.

[5]. D. Terzopoulos, *Deformable Models: Classic, Topology-Adaptive and Generalized Formulations*, ch.2.

[6]. L.D. Cohen, On Active Contour Models and Balloons, *Computer Vision, Graphics and Image Processing: Image Understanding* 53(2), 211-218.

[7]. C. Xu and J. Prince, Gradient Vector Flow: A New External Force for Snakes, *IEEE Proc. Conf. on Comp. Vis. Patt. Recog*, 1997, 66-71.

[8]. C. Xu, J. Prince, Snakes, Shapes and Gradient Vector Flow, *IEEE Transactions on Image Processing*, Vol 7, No 3, 1998.

[9]. C. Xu, J.L. Prince, Generalized gradient vector flow external forces for active contours, *Signal Processing* 7(1), 1998, 131-139.

[10]. C. Xu and J. Prince, Gradient Vector Flow Deformable Models, in: *Handbook of Medical Imaging*, Academic Press, 2000.

[11]. T. Mcinerney, *Topologically Adaptable Deformable Models For medical Image Analysis*, Ph.D Dissertation, University of Toronto, 1997.

[12]. T. McInerney and D. Terzopoulos, Medical Image Segentation Using Topologically Adaptable Surfaces, *Proc. CVRMed'97*, France, 1997.

[13]. T. McInerney and D. Terzopoulos, Topology Adaptive Deformable Surfaces for Medical Image Volume Segmentation, *IEEE Transactions on Medical Imaging*, Vol 18, No 10, October 1999, 840-850.

[14]. T. McInerney and D. Terzopoulos, T-snakes: Topology adaptive snakes, *Medical Image Analysis* 4, 2000, 73-91.

[15]. Takashi Ida, Yoko Sambonsugi, Self-Affine Mapping System and Its Application to Object Contour Extraction, *IEEE TRANCACTIONS ON IMAGE PROCESSING*, Vol. 9, No 11, 2000.

[16]. Takashi Ida, Yoko Sambonsugi and Toshiaki Watanabe, Boundary Fitting of extracted Objects Using LIFS, *System and Computers in Japan*, Vol. 31, No.8, 2000.

[17]. Thomas Walter and Jean-Claude Klein, "Segmentation of Color Fundus Images of the Human Retina: Detection of the Optic disk and the Vascular Tree Using Morphological Techniques", 2001.

[18]. Huiqi Li and Opas Chutatape, "Fundus Image Features Extraction", Proceedings of the 22nd Annual EMBS International Conference, 2000.

[19]. Huiqi Li and Opas Chutatape, "AUTOMATIC LOCATION OF OPTIC DISK IN RETINAL IMAGES", IEEE 2001.

[20]. Alireza Osareh, Majid Mirmehdi, Barry Thomas and Richard Markham, "Colour Morphology and Snakes for Optic Disc Localisation", 2002.

[21]. P. L. Rosin, D. Marshall and J. E. Morgan, “Multimodal retinal imaging: New strategies for the ditection of glaucoma”, IEEE ICIP 2002.

Figure captions

Figure 1. a) Final contours with $n = 8$ (curve a) and $n = 32$ (curve β), b) Final contour using the adapting scheme (curve β), curve a is the initial contour.

Figure 2. Initial (curve a) and final (curve β) optic disk contour using the adapting scheme and MD as optimization criterion.

Figure 3. Optic disk extraction with a) the classical snake (α=2, β=2, w=7, w_p=0.05, 125 total iterations), b) GVF snake (α=2, β=2, w=7, w_p=0.05, μ=0.29, 80 iterations for GVF calculation and 125 total iterations), c) T-snake (α=20, β=20, w=71, w_p=70, 45 total iterations), d) self-affine mapping system (e_{min}=4, e_{max}=32, r=2).

Figure 4. Cross-correlation coefficients for the four deformable model techniques and for the 26 retinal images

Figure 5. Total segmentation time for the four deformable model algorithms for the 26 retinal images

Figure 6. Examples of contour initialization for a) the classical snake and gvf snake and b) the self-affine mapping system

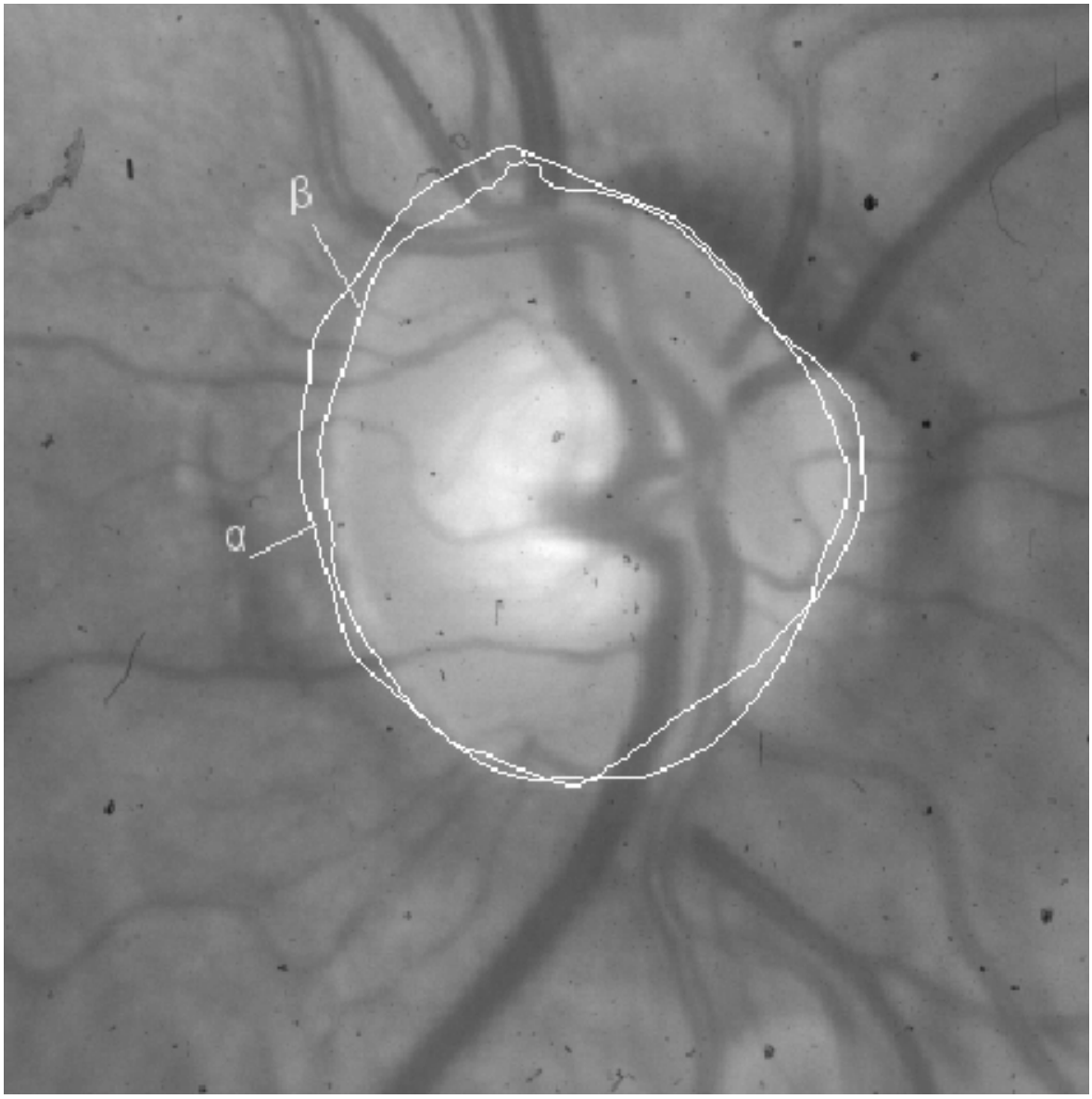

Fig. 1a

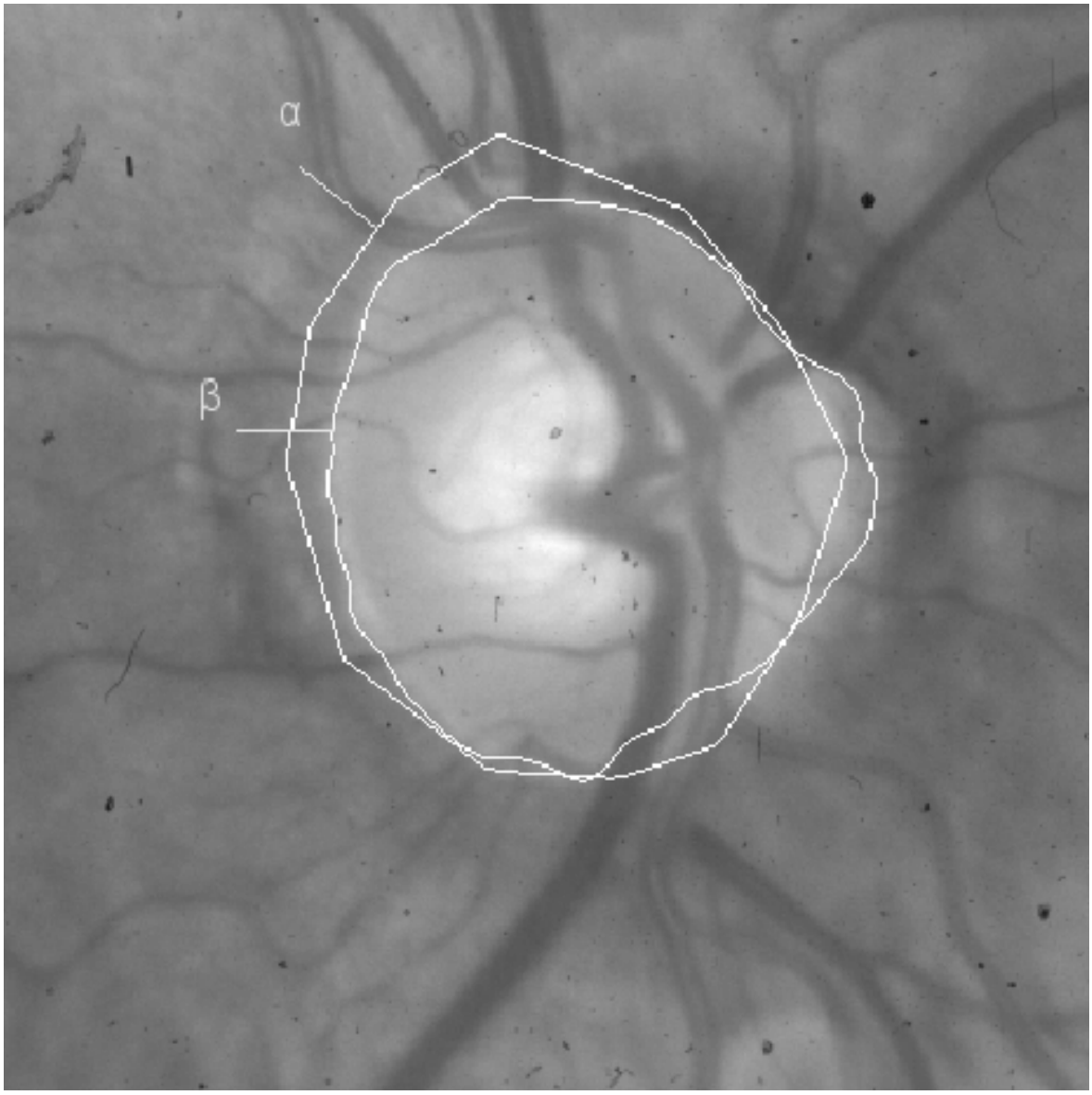

Fig. 1b

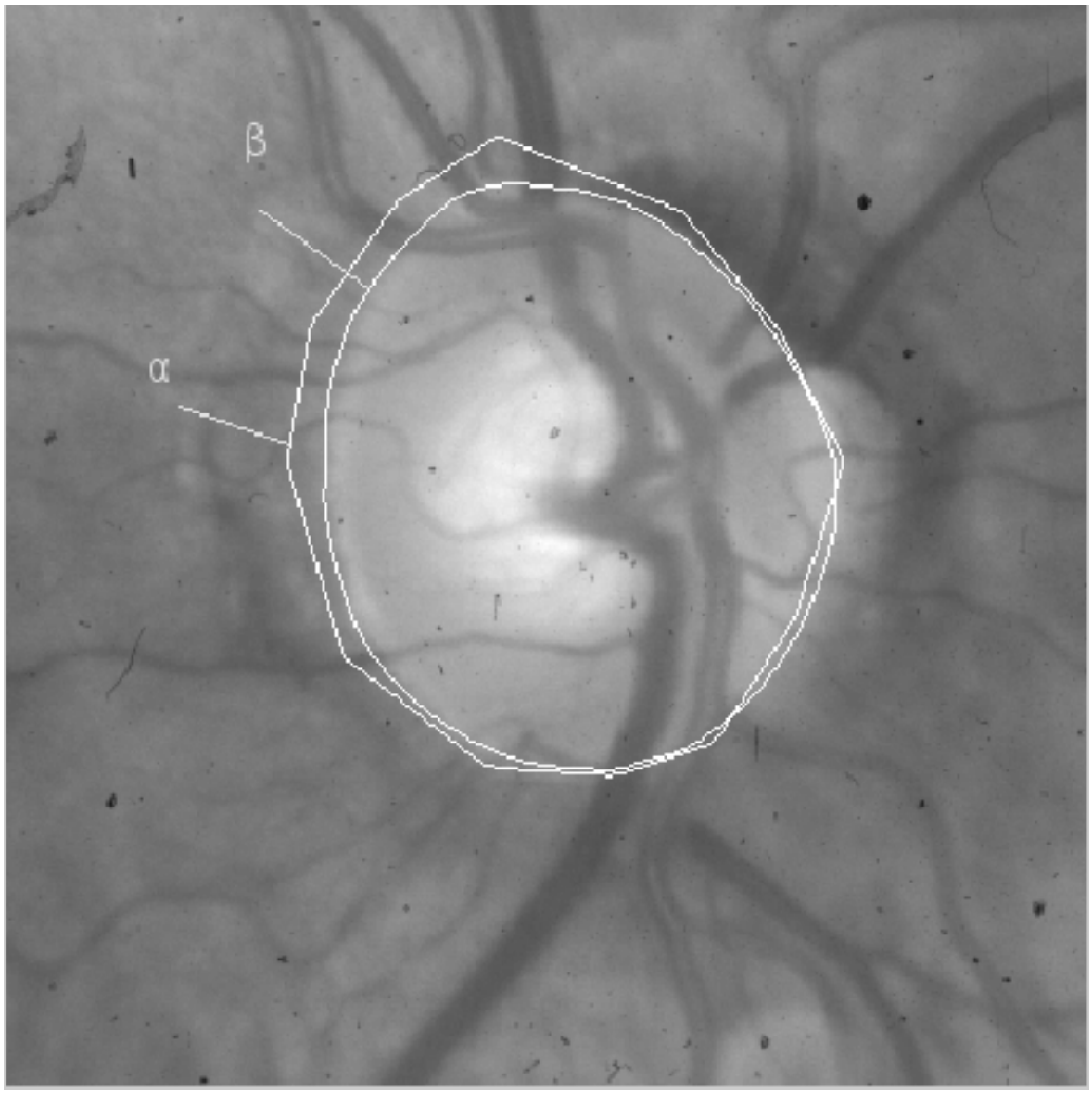

Fig. 2

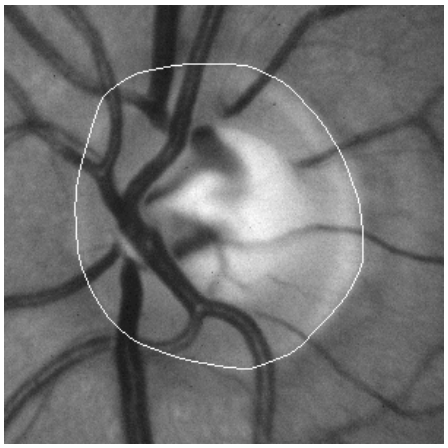

a

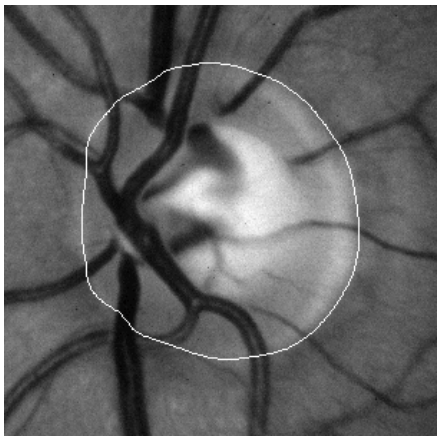

b

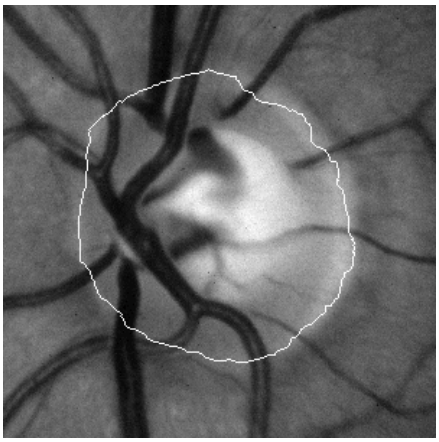

c

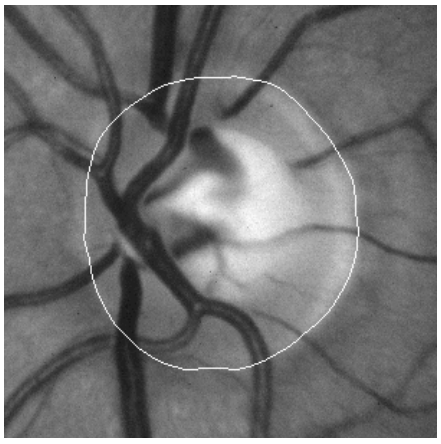

d

e

Fig. 3

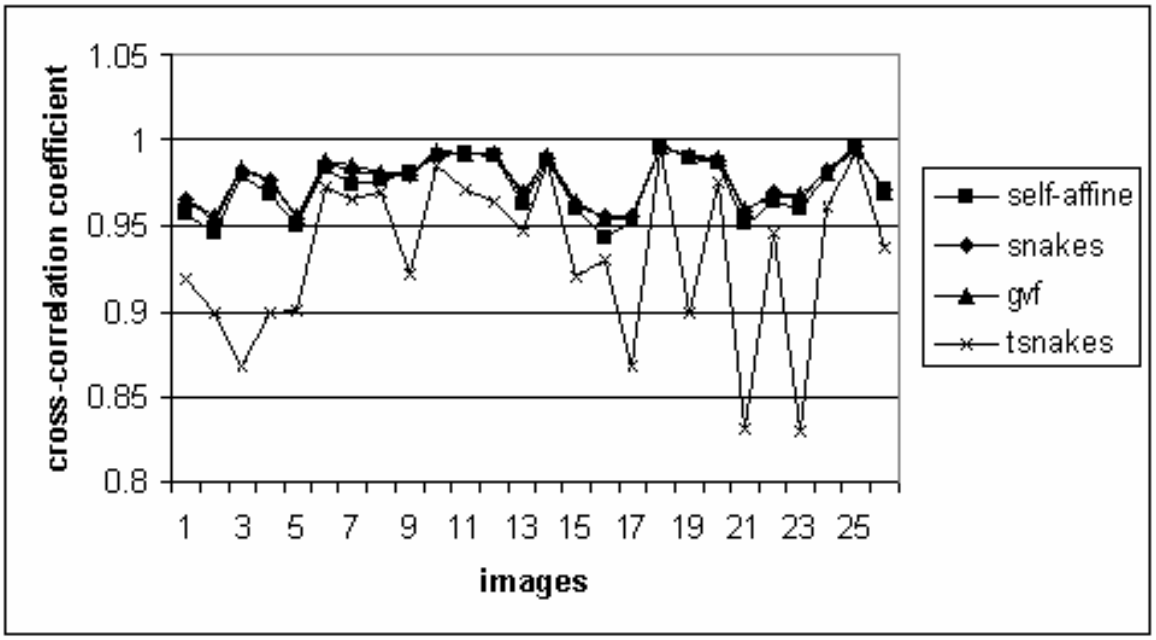
cross-correlation coefficient
1.05
1
0.95
0.9
0.85
0.8
1
3
5
7
9
11
13
15
17
19
21
23
25
images
self-affine
snakes
gvf
tsnakes

Fig. 4

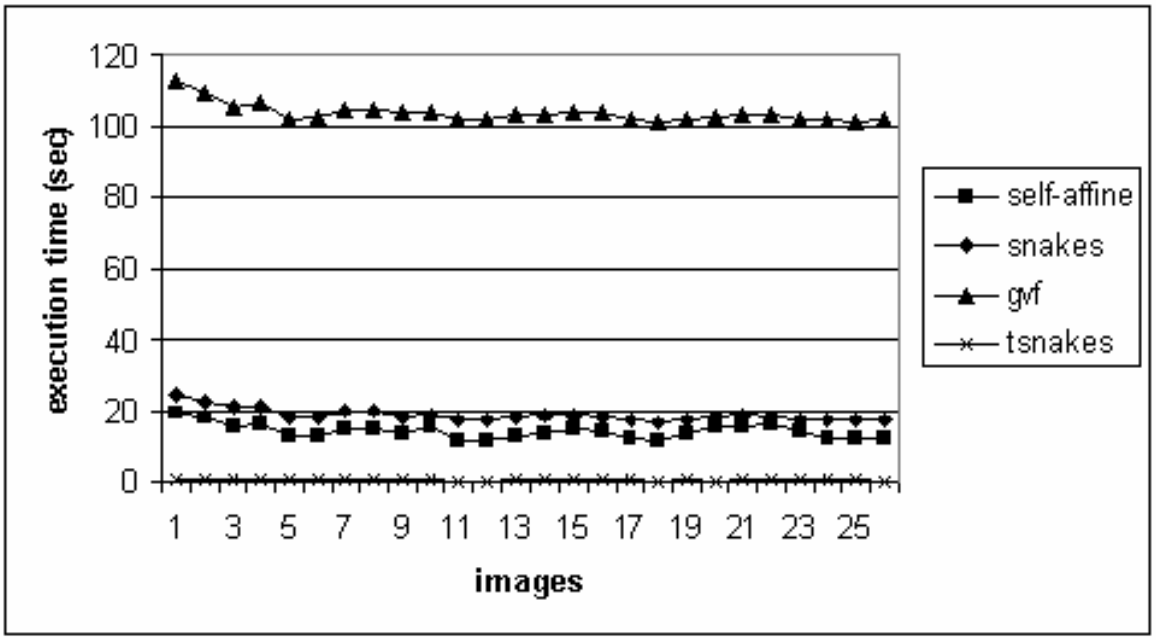
120
100
80
60
40
20
0
execution time (sec)
1
3
5
7
9
11
13
15
17
19
21
23
25
images
self-affine
snakes
gvf
tsnakes

Fig. 5

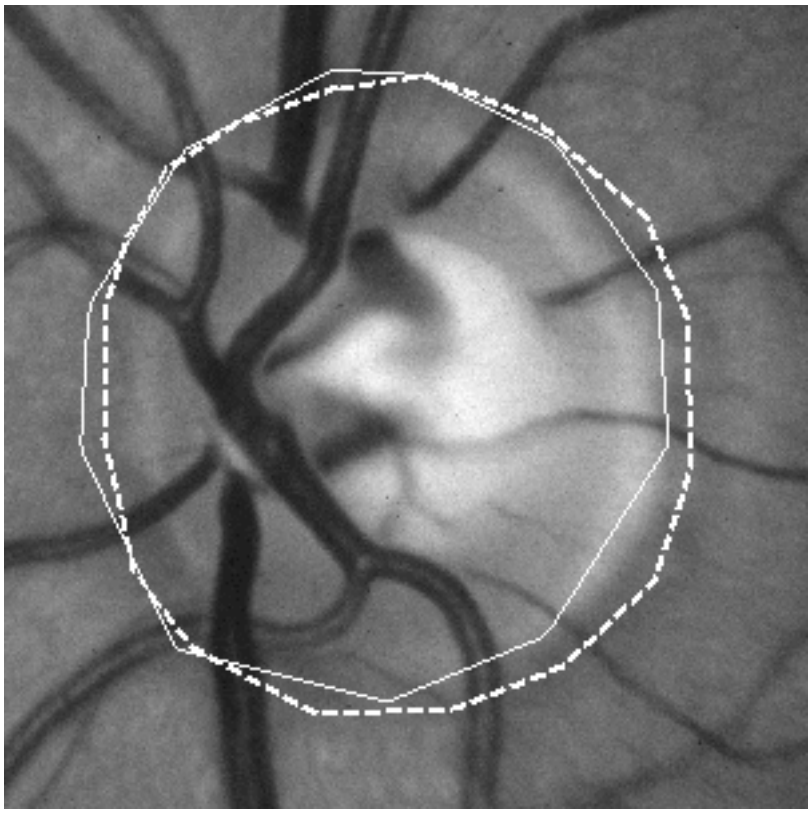

a

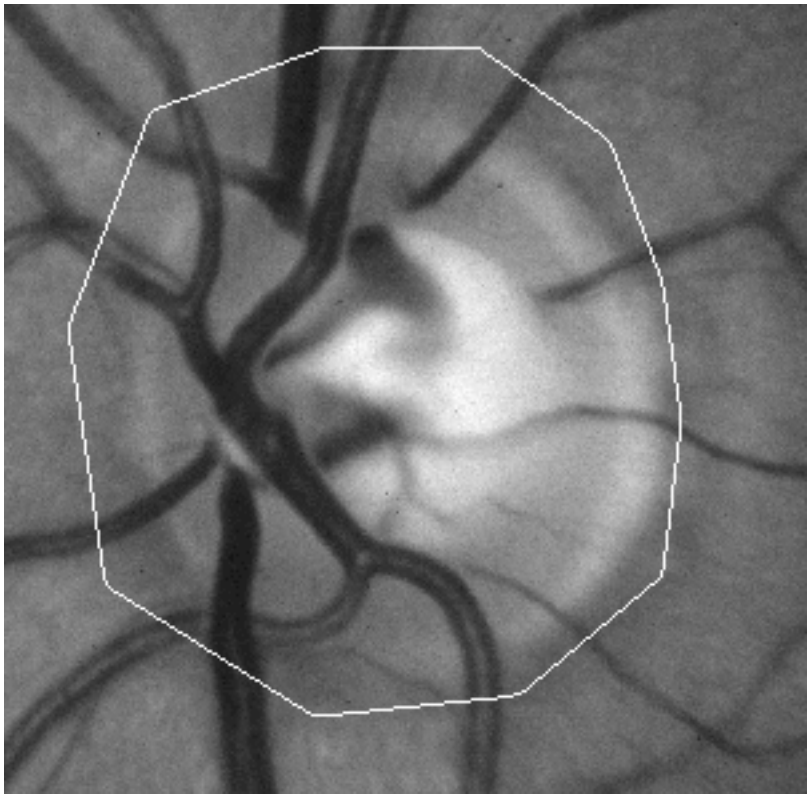

b

Fig. 6